ACES Asian Chemical Editorial Society

DOI: 10.1002/asia.201700750

CHEMISTRY AN ASIAN JOURNAL Full Paper

Electrochemistry

Controllable Synthesis of Ultrathin $NiCo_2O_4$ Nanosheets Incorporated onto Composite Nanotubes for Efficient Oxygen Reduction

Yunpeng Huang,[a] Fen Cui,[b] Yan Zhao,[a] Jian Bao,[a] Jiabiao Lian,[a] Yuanguo Xu,[b] Tianxi Liu,*[c] and Huaming Li*[a, b]

Abstract: Exploring non-precious-metal-based oxygen reduction reaction (ORR) electrocatalysts featuring high efficiency, low cost, and environmental friendliness is of great importance for the broad applications of fuel cells and metal–air batteries. In this work, ultrathin $NiCo_2O_4$ nanosheets deposited on 1D SnO_2 nanotubes (SNT) were successfully fabricated through a productive electrospinning technique followed by a sintering and low-temperature coprecipitation strategy. This hierarchically engineered architecture has ultrathin $NiCo_2O_4$ nanosheets uniformly and fully erected on both walls of tubular SNTs, which results in improved electrochemical activity as an ORR catalyst, in terms of positive onset potential and high current density, as well as superior tolerance to crossover effects and long-term durability with respect to the commercial Pt/C catalyst. The excellent performance of SNT@$NiCo_2O_4$ composites may originate from their rationally designed hierarchical tubular nanostructure with completely exposed active sites and interconnected 1D networks for efficient electron and electrolyte transfer; this makes these composite nanotubes promising candidates to replace platinum-based catalysts for practical fuel cell and metal–air battery applications.

Introduction

The growing demand for clean and sustainable energy resources have motivated vigorous exploration for advanced energy storage and conversion technologies, namely, fuel cells, metal–air batteries, lithium-ion batteries, and supercapacitors. Among the front runners, fuel cells and metal–air batteries have raised great expectations as ideal energy conversion systems owing to their environmental friendliness and high efficiency, in which the electrochemical oxygen reduction reaction (ORR) on the cathode plays a key role.[1–6] Generally, platinum-based electrocatalysts exhibit the best overall ORR performance, but their high cost, poor durability, and severe crossover effects are significant obstacles to the large-scale commercialization of platinum-based electrocatalysts.[7] Therefore, it is highly desirable to develop non-precious-metal-based electrocatalysts with excellent catalytic activity, long-term stability, and superior methanol tolerance.

Recently, iron- or cobalt-based electrocatalysts have attracted much research interest in electrochemical catalysis to replace traditional platinum-based catalysts.[8–12] In particular, cobalt-based mixed transition-metal oxides (MTMOs) have captured growing interests because of their remarkable electrochemical activity and low cost. $NiCo_2O_4$ nanomaterials with various morphologies, such as nanotubes,[13] nanoneedles,[14] and nanoplates,[15] nanospheres,[16] have been synthesized,[17] which manifest excellent electrocatalytic activities. Cao et al. fabricated 3D $NiCo_2O_4$ sheets with abundant macropores and high surface area to decrease the mass transfer resistance during the electrochemical process; thus resulting in improved ORR catalytic performance in alkaline solution.[18] In spite of the advantages, the relatively low electrical conductivity, limited number of active sites, and rare available surface area are still great challenges that limit the electrocatalytic activity of $NiCo_2O_4$. To solve these problems, a prospective approach is to construct conductive composites. By combining $NiCo_2O_4$ with highly conductive substrates (e.g., carbon nanotubes, graphene), the electron-transfer capability of the composites can be largely enhanced during the ORR process. For example, Lou et al. developed a facile two-step strategy to grow $NiCo_2O_4$ nanosheets on conductive graphene sheets;[19] the obtained hybrid catalyst exhibited high activity for the ORR, in terms of low overpotential and high current density. Another approach is to rationally

[a] Dr. Y. Huang, Dr. Y. Zhao, Dr. J. Bao, Dr. J. Lian, Prof. Dr. H. Li
Institute for Energy Research, Jiangsu University
Zhenjiang, 212013 (P.R. China)
E-mail: lhm@ujs.edu.cn

[b] F. Cui, Dr. Y. Xu, Prof. Dr. H. Li
School of Chemistry and Chemical Engineering
Jiangsu University, Zhenjiang, 212013 (P.R. China)

[c] Prof. Dr. T. Liu
State Key Laboratory for Modification
of Chemical Fibers and Polymer Materials
College of Materials Science and Engineering
Donghua University, Shanghai 201620 (P.R. China)
E-mail: txliu@dhu.edu.cn

Supporting information and the ORCID identification number(s) for the author(s) of this article can be found under https://doi.org/10.1002/asia.201700750.

design porous nanostructures or ultrathin nanoparticles that can provide more electrochemical active sites and short ion/electron transport paths to facilitate an efficient ORR process. Guo and co-workers reported the successful preparation of mesoporous $NiCo_2O_4$ nanoplate arrays on 3D graphene foam.[20] By virtue of the fully exposed $NiCo_2O_4$ active edges and increased accessible surface area, this hierarchical nanomaterial manifested outstanding ORR performance with the four-electron process in alkaline media.

Tubular nanostructures are one of the most attractive nanoachitectures owing to their 1D configuration and greatly increased surface area with respect to that of solid nanofibers/nanowires (NWs).[21,22] Li et al. fabricated magnetic $ZnFe_2O_4$/ZnO nanotubes through electrospinning and calcination processes.[23] Owing to the multiporous structure and enhanced specific surface area of the composites, $ZnFe_2O_4$/ZnO nanotubes show excellent photocatalytic activity towards dye decolorization. Similarly, α-Fe_2O_3 nanotubes were also synthesized by using the same electrospinning technique.[21] These nanotubes were utilized as growing templates for the uniform deposition of MnO_2 nanosheets. Such a tubular hierarchical architecture can provide a short ion diffusion pathway and effective electrical contact during the electrochemical process. Therefore, hierarchical tubular nanoarchitectures composed of porous $NiCo_2O_4$ with sufficient exposed active sites are considered as desirable non-precious-metal-based ORR catalysts.

SnO_2 is a conventional metal oxide semiconductor with exceptional electrochemical properties.[24,25] SnO_2 nanotubes (SNTs) constructed from nanosized particles that can be facilely prepared through a simple calcination of electrospun polymer nanofibers containing SnO_2 precursors.[26–28] On the basis of the above considerations, we propose herein the controllable preparation of ultrathin $NiCo_2O_4$ nanosheets that are incorporated onto SNTs with 3D hierarchical nanostructures through a versatile low-temperature coprecipitation strategy.

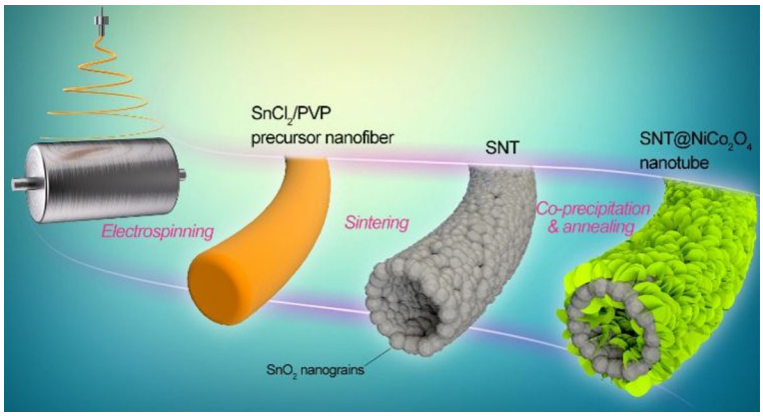

Scheme 1. Preparation procedure used to obtain the SNT@$NiCo_2O_4$ composite nanotubes. PVP = polyvinylpyrrolidone.

Results and Discussion

Synthesis of SNT@$NiCo_2O_4$ Nanotubes

SNTs composed of numerous SnO_2 nanograins were first synthesized through sintering of electrospun precursor nanofibers, which possessed high specific surface area and interconnected 1D networks (Scheme 1). Ultrathin $NiCo_2O_4$ nanosheets were then uniformly deposited on both walls of the SNTs with their active edges fully exposed. Through the rational construction of hierarchical SNT@$NiCo_2O_4$ composite nanotubes, the electrochemically active sites can be drastically improved, and the electron-transfer efficiency is expected to be greatly promoted. Therefore, as-prepared SNT@$NiCo_2O_4$ nanotubes manifest remarkable ORR electrocatalytic activity, in terms of low onset potential and high tolerance to methanol, which ensures that these composite nanotubes have great potential as platinum-free electrodes in future fuel cell and metal–air battery applications.

Morphology and Structure of SNT@$NiCo_2O_4$ Nanotubes

Electrospinning is a simple yet effective strategy for producing uniform polymer nanofibers containing different doping agents. As revealed in Figure S1 in the Supporting Information, randomly oriented $SnCl_2$/PVP precursor nanofibers with uniform diameter distribution are prepared successfully. After being sintered at 550 °C to decompose the PVP component, SNT nanomaterials can be readily obtained during high-temperature pyrolysis, according to the Kirkendall effect.[29] Figure 1 A presents interconnected 1D SNTs with well-defined tubular structure and rough surface. In particular, individual SNTs are composed of numerous SnO_2 nanograins with a mean diameter of 30 nm (Figure 1 B). These unique dual-surface nanostructures will definitely increase the specific surface area and provide sufficient nucleation sites for the subsequent construction of hierarchical structures. As proved by the BET analysis in Figure S2 in the Supporting Information, the specific surface area of SNT nanomaterial is 60 $m^2 g^{-1}$, which is much higher than that of conventional electrospun nanofibers. Additionally, the total pore volume of neat SNTs is 0.13 $cm^3 g^{-1}$, and the pore diameter range is determined to be 2 to 18 nm by the Barret–Joyner–Halenda (BJH) method (inset of Figure S2 in the Supporting Information).

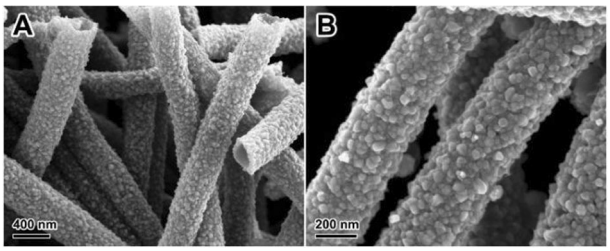

Figure 1. Field-emission (FE) SEM images of SNT at A) low and B) high magnifications.

An environmentally friendly, low-temperature coprecipitation method followed by annealing treatment was used to grow $NiCo_2O_4$ nanosheets on SNTs. Composites with different $NiCo_2O_4$ percentages were prepared by varying the reaction time (2, 4, and 6 h, corresponding products were denoted as SNT@$NiCo_2O_4$-1, SNT@$NiCo_2O_4$-2, and SNT@$NiCo_2O_4$-3, respectively). After 2 h of reaction, only inconspicuous little whiskers of $NiCo_2O_4$ could barely be observed scattered on the surface of SNTs (Figure 2A and D), indicating the initial stage of reaction. For the case of SNT@$NiCo_2O_4$-2 composites, it can be clearly observed from Figure 2B and E that the SNTs are uniformly covered with deposits of sheet-like $NiCo_2O_4$ nanoparticles on both inner and outer walls. It is also noteworthy that the $NiCo_2O_4$ nanosheets are vertically grown with their active edges totally exposed outward. These results indicate that 4 h is suitable for the coprecipitation reaction. Elemental mapping results shown in Figure S3 in the Supporting Information reveal the corresponding elements in the SNT@$NiCo_2O_4$-2 composite. Upon further prolonging the reaction time to 6 h, the relatively thin $NiCo_2O_4$ sheets in SNT@$NiCo_2O_4$-2 turn into thick $NiCo_2O_4$ plates. As shown in Figure 2C and F, SNT@$NiCo_2O_4$-3 is covered with larger $NiCo_2O_4$ plates that possess much fewer useful active sites with respect to that of SNT@$NiCo_2O_4$-2. The well-defined hierarchical tubular nanostructure of SNT@$NiCo_2O_4$-2 was also inspected by TEM (Figure 3), through which $NiCo_2O_4$ nanosheets were confirmed to be uniformly distributed on SNT templates. Additionally, from the sharp contrast of the nanosheet in the inset of Figure 3, the thickness of $NiCo_2O_4$ nanosheets is speculated to be ultrathin. The morphology of pure $NiCo_2O_4$ nanosheets was also observed by SEM (Figure S4 in the Supporting Information) to exhibit a thick hexagonal shape with a mean diameter of about 900 nm; this indicates that SNTs with numerous nucleation sites could be the perfect substrate for the direct uniform growth of $NiCo_2O_4$ nanosheets.

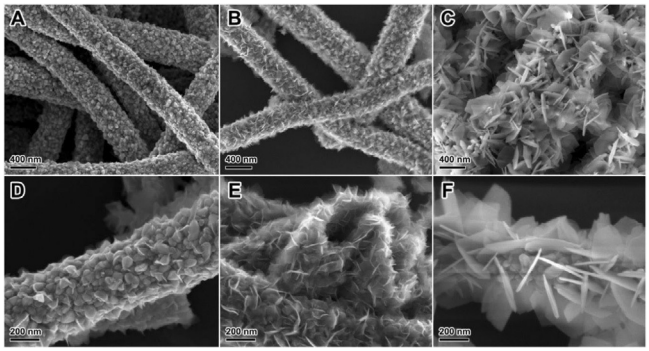

Figure 2. FESEM images of SNT@$NiCo_2O_4$-1 (A, D), SNT@$NiCo_2O_4$-2 (B, E), and SNT@$NiCo_2O_4$-3 (C, F) at different magnifications.

The crystal structures of synthesized SNTs, $NiCo_2O_4$, and SNT@$NiCo_2O_4$-2 composites were investigated by means of XRD. As shown in Figure 4, a series of diffraction peaks attributed to the rutile structure of SnO_2 (JCPDF, card no. 77-0450) can be observed. For the pure $NiCo_2O_4$ sample (Figure 4B), the

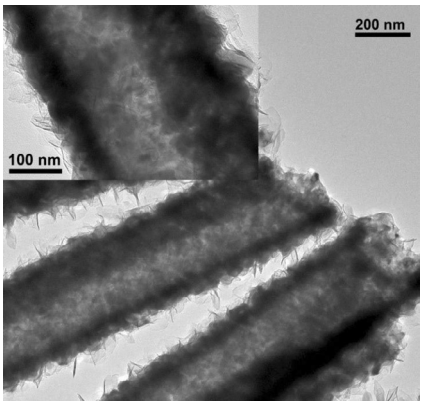

Figure 3. TEM images of SNT@$NiCo_2O_4$-2. Inset shows the magnified view of $NiCo_2O_4$ nanosheets.

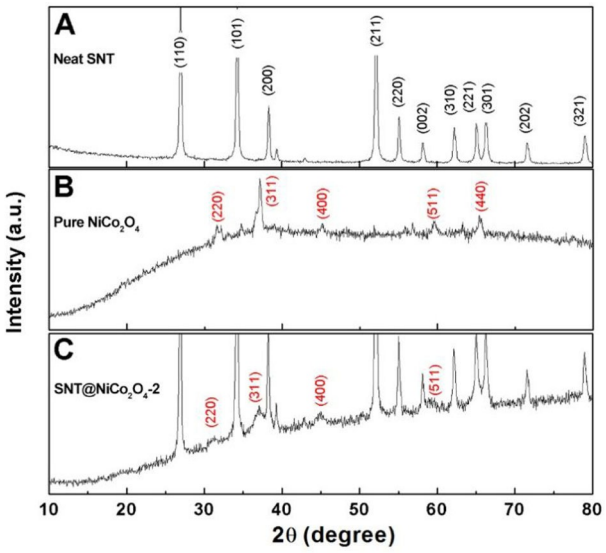

Figure 4. XRD patterns of A) neat SNTs, B) pure $NiCo_2O_4$ nanosheets, and C) SNT@$NiCo_2O_4$-2 composites.

detected peaks at $2\theta = 31.5$, 36.9, 45.1, 59.6, and 65.5° can be assigned to the (220), (311), (400), (511), and (440) planes, respectively, in the spinel structure of $NiCo_2O_4$ (JCPDF, card no. 20-0781). For SNT@$NiCo_2O_4$-2 composites, the (220), (311), (400), and (511) crystal planes can be clearly observed in the spectrum of Figure 4C, which indicates the successful deposition of $NiCo_2O_4$ on SNTs. The invisibility of the (440) diffraction peak may be caused by the much higher intensity of SNT peaks.

X-ray photoelectron spectroscopy (XPS) characterization was performed to confirm the elemental composition and oxidation state of SNT@$NiCo_2O_4$-2 composites. As shown in Figure 5, characteristic peaks of nickel, cobalt, tin, and oxygen can be clearly observed in the survey spectrum; the carbon signal may originate from the carbon-based residue. The core-level spectrum of Co 2p can be deconvoluted into four peaks: the peaks at 782.6 and 797.5 eV are attributed to Co^{2+}, whereas those at 780.5 and 795.3 eV are ascribed to Co^{3+}. For the Ni 2p spectrum, the fitting peaks at 855.7 and 873.3 eV are as-

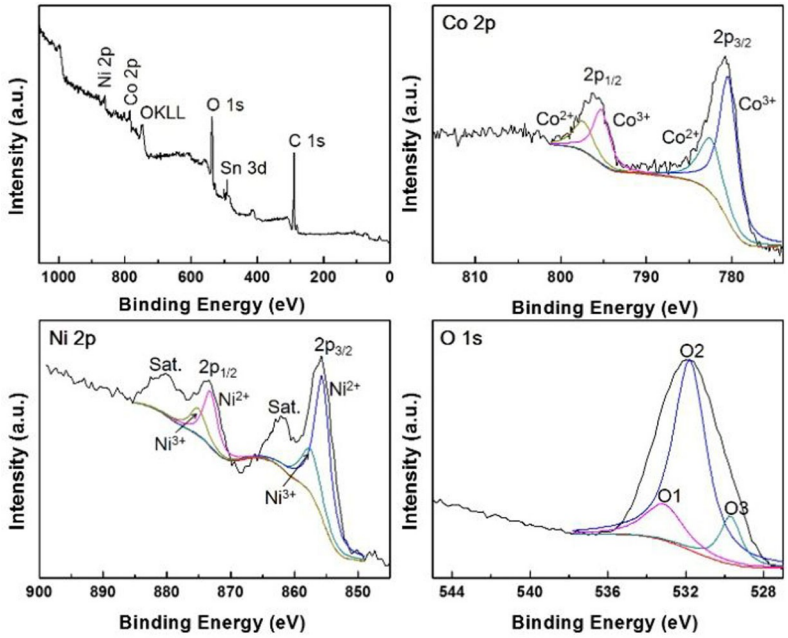

Figure 5. XPS survey spectrum and core-level spectra of Co 2p, Ni 2p, and O 1s.

signed to Ni^{2+}, whereas the other two fitting peaks at 857.8 and 875.4 eV can be indexed to Ni^{3+}. The satellite peaks located beside Ni $2p_{1/2}$ and Ni $2p_{3/2}$, that is, 861.9 and 880.2 eV, are two shakeup peaks of nickel.[30] Meanwhile, the high-resolution spectrum of O 1s is attributed to three oxygen types. The O1 peak at 533.2 eV is a typical metal–oxygen bonds, whereas the O2 peak at 531.8 eV is caused by functional groups such as hydroxyl or carboxyl. The O3 peak at 529.7 eV can be assigned to physically or chemically absorbed H_2O on the surface.[31,32] Moreover, precise compositional analysis indicates that the surface atomic ratio of Ni/Co/O is 1:2.1:4.2, which is consistent with the formula $NiCo_2O_4$. The above results further confirm the successful fabrication of SNT@$NiCo_2O_4$ composites.

To further determine the precise percentage of $NiCo_2O_4$ nanomaterials deposited on SNTs, thermogravimetric analysis (TGA) was performed under a flow of air to give the results provided in Figure 6. It is noteworthy that the product of the coprecipitation reaction is NiCoLDH, the precursor of $NiCo_2O_4$, which must be annealed to form well-crystallized spinel $NiCo_2O_4$. As shown in the TGA curve of NiCoLDH, the weight loss of 16% is attributed to the dehydration and decomposition of NiCoLDH, from which all intercalated H_2O molecules escaped completely from the interlayer space. Based on the weight loss of the precursors of SNT@$NiCo_2O_4$-1, SNT@$NiCo_2O_4$-2, and SNT@$NiCo_2O_4$-3 (denoted as SNT@NiCoLDH-1, SNT@NiCoLDH-2, SNT@NiCoLDH-3, respectively), namely, 1.1, 4, and 9.5%, respectively, the loading percentage of $NiCo_2O_4$ is calculated to be 5, 19, and 47.8%, respectively.

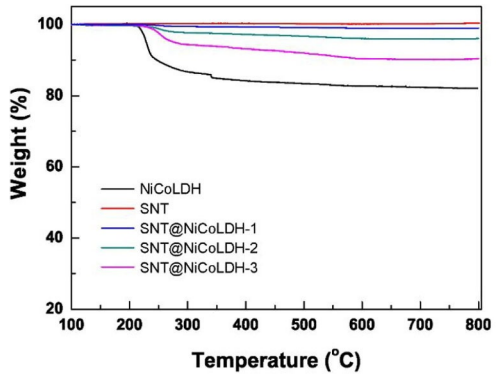

Figure 6. TGA results for SNT@NiCoLDH composites, SNTs, and NiCoLDH (the precursor of $NiCo_2O_4$).

Electrochemical ORR Tests of Catalysts

The catalytic activity of SNT@$NiCo_2O_4$ composites, neat SNTs, and pure $NiCo_2O_4$ towards the ORR was first tested by cyclic voltammetry (CV) in an oxygen-saturated 0.1 M aqueous KOH electrolyte at a scan rate of 10 mV s^{-1}. As shown in Figure 7A, all samples exhibit well-defined cathodic redox peaks that correspond to the oxygen reduction process in electrolyte. A more positive peak potential, along with larger peak current density, indicates better ORR activity. Clearly, neat SNTs show negligible electrochemical activity; NiCoLDH also presents weak activity before further heat treatment (Figure S5 in the Supporting Information), whereas pure $NiCo_2O_4$ sheets exhibit significant ORR activity with a more positive peak potential owing to the intrinsic electrochemical activity of spinel $NiCo_2O_4$. To optimize the loading percentage of $NiCo_2O_4$ nanosheets in SNT@$NiCo_2O_4$ composites, the CV curves of SNT@$NiCo_2O_4$-1, SNT@$NiCo_2O_4$-2, and SNT@$NiCo_2O_4$-3 were also collected. Upon increasing the loading amount of $NiCo_2O_4$ nanosheets, the peak potential of the composites rises first then falls; this indicates the best ORR activity of SNT@$NiCo_2O_4$-2. Furthermore, LSV curves of SNT@$NiCo_2O_4$-2 also shows a more positive onset potential and larger current density with respect

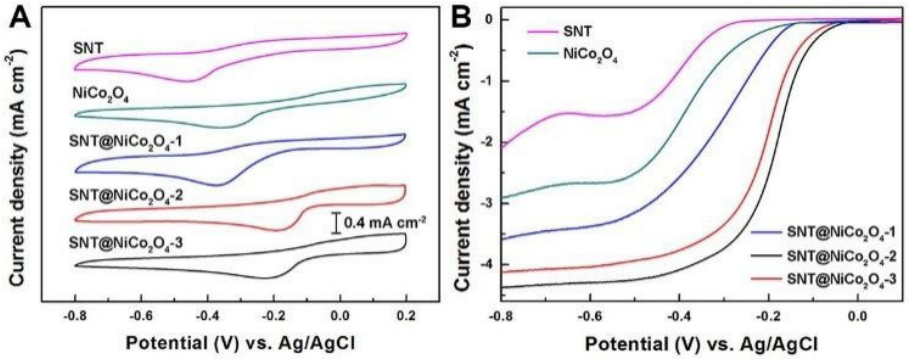

Figure 7. A) CV curves of different samples in oxygen-saturated 0.1 M aqueous KOH electrolyte at a scan rate of 10 mV s^{-1}. B) Linear sweep voltammetry (LSV) curves of different samples in oxygen-saturated 0.1 M KOH at a scan rate of 5 mV s^{-1} at 1600 rpm.

to those of SNT@$NiCo_2O_4$-1 and SNT@$NiCo_2O_4$-3 (Figure 7B); this confirms the optimized growth of $NiCo_2O_4$ on SNT@$NiCo_2O_4$-2. Specifically, the uniform distribution of ultrathin $NiCo_2O_4$ nanosheets on both walls of SNTs could deliver abundant electrochemically active sites for SNT@$NiCo_2O_4$-2, whereas the deposition of $NiCo_2O_4$ on SNT@$NiCo_2O_4$-1 and SNT@$NiCo_2O_4$-3 is either scarce or excessive; thus leading to the superior ORR catalytic activity of SNT@$NiCo_2O_4$-2. It is also worth noting that SNT@$NiCo_2O_4$-2 exhibits much better ORR activity than that of pure $NiCo_2O_4$ sheets; this can probably be ascribed to fast electron transfer facilitated by the interconnected network of 1D tubular nanostructures. Electrochemical impedance spectroscopy (EIS) results for SNT@$NiCo_2O_4$-2 and $NiCo_2O_4$ further confirm the above speculation. As shown in Figure S6 in the Supporting Information, the series resistance (R_s, x intercept of the EIS spectra) and the charge-transfer resistance (R_{ct}, semicircles in the high-frequency region of the spectra) of pure $NiCo_2O_4$ nanosheets decrease greatly after deposition on SNTs; this indicates that the SNT backbone can accelerate ion diffusion and charge transfer during the electrochemical reaction.

To compare the ORR performance of SNT@$NiCo_2O_4$-2 and Pt/C catalyst, CV measurements were recorded (Figure 8A). No significant peaks can be observed between −0.8 and 0.2 V for either electrode. When O_2 was introduced into the cell, the SNT@$NiCo_2O_4$-2 catalyst exhibits excellent ORR activity with a reduction peak at −0.17 V, which outperforms most previously reported ORR catalysts (Table 1), although inferior to that of the Pt/C catalyst with a near-zero peak potential at −0.08 V. To further evaluate the ORR catalytic performance of SNT@$NiCo_2O_4$-2, Pt/C, and pure $NiCo_2O_4$, LSV measurements were conducted at various rotating speeds in oxygen-saturated 0.1 M KOH electrolyte at a scan rate of 10 mV s^{-1}. As shown in Figure 8B and Figures S7A and S8A in the Supporting Information, the current density of SNT@$NiCo_2O_4$-2, Pt/C, and $NiCo_2O_4$-modified rotating disk electrodes (RDEs) increases upon raising the rotating speed from 400 to 2025 rpm; this can be ascribed to the shortened diffusion distance for electron transfer at

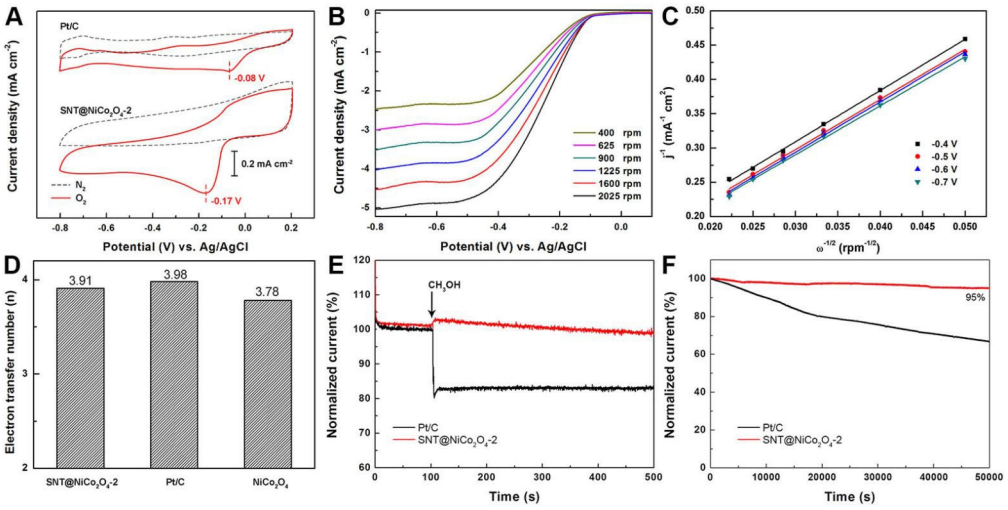

Figure 8. A) CV curves of SNT@$NiCo_2O_4$-2 and Pt/C electrodes in oxygen- and nitrogen-saturated 0.1 M KOH electrolyte at a scan rate of 10 mV s^{-1}. B) LSV curves of SNT@$NiCo_2O_4$-2 electrode in oxygen-saturated 0.1 M KOH at different rotating rates with a scan rate of 5 mV s^{-1}. C) Corresponding Koutecky–Levich (K-L) plots of SNT@$NiCo_2O_4$-2 at −0.4, −0.5, −0.6, and −0.7 V. D) Electron-transfer numbers of different electrodes derived from their corresponding K-L plots. Chronoamperometric responses of SNT@$NiCo_2O_4$-2 and Pt/C electrodes: E) methanol crossover tests by addition of methanol to the electrochemical cell at 100 s; F) long-term stability tests for 50000 s.

Table 1. Comparison of the ORR performance of different cobalt-based catalysts.[a]

Catalyst	Electrolyte	Reduction peak (V vs. Ag/AgCl)	Half-wave potential (V vs. Ag/AgCl)	Ref.
$[CoN_4]_3$/C	0.1 M KOH	−0.26	N/A	[33]
NCF-Co[a]	0.1 M KOH	−0.17	−0.18	[34]
macroporous $NiCo_2O_4$ sheet	0.1 M KOH	−0.21	−0.22	[15]
$NiCo_2O_4$ NWs	0.1 M KOH	−0.37	−0.3	[35]
$NiCo_2O_4$-rGO	0.1 M KOH	−0.349	N/A	[16]
SNT@$NiCo_2O_4$ nanotube	0.1 M KOH	−0.17	−0.21	this work

[a] NCF-Co: nitrogen-doped carbon fibers (NCFs) decorated with cobalt nanoparticles; r-GO: reduced graphene oxide; N/A: not applicable.

high speed. The corresponding K-L plots (j^{-1} vs. $\omega^{-1/2}$) of all catalysts were obtained from LSV curves at different potentials (Figure 8C and Figures S7B and S8B in the Supporting Information). All plots exhibited perfect linearity, which indicated first-order reaction kinetics towards oxygen for SNT@$NiCo_2O_4$-2, Pt/C, and pure $NiCo_2O_4$. The average electron-transfer number (n) during the electrochemical ORR process for all three electrodes was calculated to be 3.91, 3.98, and 3.78, respectively, according to Equation (1) (see the Experimental Section and Figure 8D); thus the SNT@$NiCo_2O_4$-2 catalyst favors a more efficient four-electron ORR process. While the less efficient ORR catalytic performance of pure $NiCo_2O_4$ is probably attributed to the limited accessibility of ion/electron within the $NiCo_2O_4$ agglomerates (Figure S2 in the Supporting Information). To further evaluate the ORR pathways on SNT@$NiCo_2O_4$-2, rotating ring–disk electrode (RRDE) measurements were conducted (Figure S9 in the Supporting Information). Over the potential range investigated, the yield of HO_2^- was below 7.7% and the calculated electron transfer number was about 3.95; this was consistent with the results obtained from the K-L plots based on RDE measurements.

In practical applications, fuel molecules may travel across the electrolyte membrane and react with ORR catalysts on the cathode and deteriorate the efficiency of fuel cells; this is known as the fuel crossover effect. Hence, chronoamperometry was conducted to assess the stability of the electrodes at a fixed potential of −0.4 V in oxygen-saturated 0.1 M aqueous KOH electrolyte. As depicted in Figure 8C, when 5 M methanol is dropped into the cell at 100 s, a drastic current decrease can be observed in the ORR current of Pt/C catalyst, whereas the current of the SNT@$NiCo_2O_4$-2 electrode exhibits no visible response to methanol oxidation, which indicates superior methanol tolerance of SNT@$NiCo_2O_4$-2 with respect to that of the commercial Pt/C catalyst. Furthermore, CV curves of SNT@$NiCo_2O_4$-2 and Pt/C electrodes were also collected in oxygen-saturated 0.1 M KOH containing 2 M methanol. As observed (Figure S10A and B in the Supporting Information), the SNT@$NiCo_2O_4$-2 electrode shows a very steady current response under the interference of methanol with a small negative peak shift, whereas the CV response of the Pt/C electrode shows a strong methanol oxidation peak at around −0.125 V; this further demonstrates the high catalytic selectivity and stability of SNT@$NiCo_2O_4$-2 towards methanol. Long-term stability is another important property for the practical application of ORR catalysts. The durability of SNT@$NiCo_2O_4$-2 and Pt/C electrodes was investigated by chronoamperometric measurements under a constant potential of −0.4 V in oxygen-saturated 0.1 M KOH electrolyte at an electrode rotating speed of 1600 rpm (Figure 8F). The chronoamperometric response of the SNT@$NiCo_2O_4$-2 electrode shows excellent durability, with 95% current retention after 50000 s in the absence of any structure degradation (Figure S11 in the Supporting Information). In contrast, a decrease in current of 34% is observed for the Pt/C electrode under the same conditions.

The ORR process is intrinsically an interfacial reaction involving the adsorption and dissociation of oxygen molecules, mainly on the surface/interface of the electrode, which means that more accessible electrochemical active sites and faster migration of ion/electron potentially result in better ORR capability. Based on this idea, it is assumed that the remarkable ORR performance manifested by the SNT@$NiCo_2O_4$-2 catalyst stems from the unique tubular nanostructure with hierarchical $NiCo_2O_4$ nanosheets (Scheme 2), which can be summarized in three aspects. To begin with, tubular SNTs, with a large specific surface area, could provide substantial nucleation sites for the uniform deposition of $NiCo_2O_4$ nanosheets, which is a good start for the rational design of novel catalysts. Second, ultrathin $NiCo_2O_4$ nanosheets deposited in a vertical orientation with open structures possess numerous active sites to support an efficient ORR process. Lastly, the heterogeneous structure of SNT@$NiCo_2O_4$ composite nanotubes could ensure rapid

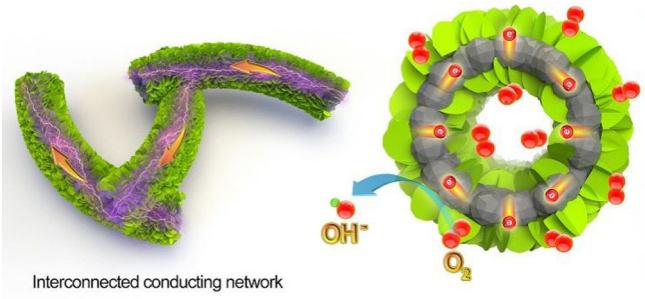

Scheme 2. Schematic representation of fast charge transfer and efficient electrolyte diffusion during the ORR process of SNT@$NiCo_2O_4$ composite nanotubes.

charge-transport kinetics, benefiting from the interconnected 1D SNT networks. The combination of these three factors results in tubular SNT@$NiCo_2O_4$ hierarchical nanotubes with excellent ORR catalytic capability.

Conclusion

A simple electrospinning strategy, followed by sintering and coprecipitation, has been proposed for the successful preparation of hierarchical SNT@$NiCo_2O_4$ tubular nanocomposites. This rationally designed 1D interconnected nanostructure not only mediated the uniform growth of $NiCo_2O_4$ nanosheets by virtue of the dual-surface SNT backbone, but also afforded efficient charge-transfer paths through the integrated networks. The resulting open structure of $NiCo_2O_4$ nanosheets with fully exposed active sites could realize fast electrolyte diffusion, leading to excellent ORR catalytic activity, in terms of a low onset potential and high current density through a four-electron reduction route, which was comparable to the Pt/C catalyst. Moreover, the SNT@$NiCo_2O_4$ nanocomposite exhibited superior tolerance to methanol crossover effects and better long-term durability with respect to Pt/C; thus it is a promising platinum-free candidate for practical fuel cell and metal–air battery applications.

Experimental Section

Materials

PVP (MW = 1 300 000 g mol^{-1}) was purchased from Sigma–Aldrich. $Co(NO_3)_2{\cdot}6H_2O$, $Ni(NO_3)_2{\cdot}6H_2O$, $SnCl_2{\cdot}2H_2O$, and hexamethylenetetramine were obtained from Sinopharm Chemical Reagent Co. Ltd. Ethanol and *N*,*N*-dimethylformamide (DMF) were supplied by Shanghai Chemical Reagent Co. Pt/C powder (20 wt% of Pt on carbon black) was obtained from Alfa Aesar.

Preparation of Hierarchical SNT@$NiCo_2O_4$ Nanotubes

The preparation process for SNT@$NiCo_2O_4$ nanotubes is presented in Scheme 1. First, SNTs with a uniform tubular structure were synthesized by a simple sintering strategy. Briefly, $SnCl_2{\cdot}2H_2O$ (1.15 g) was dissolved in a mixture of ethanol/DMF (10 mL; v/v 1/1) at room temperature, before PVP powder (1.25 g) was added to give a homogeneous gel. The as-prepared transparent mixture was pulled into a 10 mL disposable syringe and fed at an injection speed of 0.3 mm min^{-1}. A grounded aluminum roller at a rotating speed of 100 rpm was used as a collector with a receiving distance of 15 cm. When a 22 kV direct current (DC) voltage was applied to the electrospinning setup, $SnCl_2$/PVP precursor nanofibers were produced in the form of freestanding membranes. The obtained electrospun nonwoven $SnCl_2$/PVP nanofibrous membranes were sintered at 550 °C in air for 2 h to produce SNT nanomaterials.
Hierarchical SNT@$NiCo_2O_4$ nanotubes were then synthesized by a low-temperature coprecipitation method, according to a procedure reported by Lou et al. with slight modifications.[19] Typically, a transparent mixture of H_2O (40 mL) and ethanol (20 mL) containing 10 mM $Ni(NO_3)_2{\cdot}6H_2O$, 20 mM $Co(NO_3)_2{\cdot}6H_2O$, and 30 mM hexamethylenetetramine were prepared in advance at room temperature, followed by the addition of SNTs (50 mg) to obtain a fine mixture after 1 min of sonication. As-prepared grayish dispersion was treated at 90 °C under magnetic stirring for 6 h in an oil bath. When the mixture was naturally cooled to room temperature, the gray powder of SNT@NiCoLDH was collected by centrifugation and washed three times with deionized water. After annealing in air at 400 °C for 2 h at a heating speed of 2 °C min^{-1}, highly crystallized SNT@$NiCo_2O_4$ composite nanotubes were obtained. Pure $NiCo_2O_4$ was also prepared by means of the same coprecipitation method.

Characterization

FESEM (Zeiss) was utilized to observe the morphology of the samples under an acceleration voltage of 5 kV. TEM (JEOL JEM 2100) was performed under an acceleration voltage of 200 kV. Elemental distribution of the samples was determined by energy-dispersive X-ray spectroscopy (EDX). TGA was carried out under a flow of air from 100 to 800 °C at a heating rate of 20 °C min^{-1} to obtain the weight percentage of different components. XRD tests were performed on an X'Pert Pro X-ray diffractometer by using $Cu_{K\alpha}$ radiation ($\lambda = 0.1542$ nm) at an acceleration voltage of 40 kV and a current of 40 mA. XPS analyses were performed with a VG ESCALAB 220I-XL device. The specific surface area of materials was characterized with a Micro-meritics Tristar II-3020 nitrogen adsorption apparatus.

Electrochemical Measurements

The ORR catalytic performance of all catalysts was tested in N_2- or O_2-saturated 0.1 M KOH electrolyte with a typical three-electrode cell on a CHI 600 electrochemical workstation (Shanghai Chenhua Instrument Co., P.R. China), in which an Ag/AgCl electrode was set as the reference electrode; a Pt wire was the counter electrode; a modified glassy carbon electrode (GCE; 3 mm diameter), RDE (5 mm diameter), or RRDE (5.6 mm diameter) as the working electrode. In a typical procedure, the GCE and RDE were polished carefully by using an alumina slurry, followed by drying under a stream of N_2. Then, the synthesized catalyst (2 mg) and Nafion (20 μL; 5 wt% in ethanol) were dispersed in a mixture of H_2O and ethanol (1 mL; v/v 1/1) under sonication to prepare the 2 mg mL^{-1} slurry. Then, the working electrodes were obtained by casting an appropriate amount of catalyst slurry on the GCE/RDE/RRDE, which was left to dry. The specific loading amount on the GCE was set at 10 mg for CV measurements, and 20 mg on RDE for chronoamperometry and LSV measurements. The K-L plots were acquired through linear fitting of the reciprocal rotating speed versus reciprocal current density collected at different potentials. The K-L equation [Eqs. (1) and (2)] was adopted to calculate the electron transfer numbers (*n*) in the ORR process:

$$J^{-1} = J_k^{-1} + \left(B\omega^{1/2}\right)^{-1} \quad (1)$$

$$B = 0.2nFC_o D_o^{2/3} \upsilon^{-1/6} \quad (2)$$

in which J is the measured current density, J_k is the kinetic current density, ω is the electrode rotating speed in rpm, F is the Faraday constant (96 485 C mol^{-1}), C_o is the bulk concentration of O_2 in the electrolyte (1.2×10^{-6} mol cm^{-3}), D_o is the diffusion coefficient of O_2 in the electrolyte (1.9×10^{-5} cm^2 s^{-1}), ν is the kinetic viscosity of the solution (0.01 cm^2 s^{-1}), and the constant of 0.2 is used when the rotation rate is expressed in rpm. EIS was recorded over the frequency range from 0.01 Hz to 100 kHz at an amplitude of 5 mV under open-circuit potential.
For RRDE measurements, the peroxide yields and electron transfer number (*n*) could be calculated by using Equations (3) and (4), respectively:

$$HO_2^- = 200 \times \frac{I_r/N}{I_d + I_r/N} \quad (3)$$

$$n = 4 \times \frac{I_d}{I_d + I_r/N} \quad (4)$$

in which I_d is the disk current, I_r is the ring current, and N is current collection efficiency of the Pt ring (0.4).

Acknowledgements

This work is financially supported by the China Postdoctoral Science Foundation (nos. 2017M610304), the Natural Science Foundation of Jiangsu Province for Youths (no. BK20170544), the University Natural Science Research of Jiangsu (no. 17KJB430010), the National Natural Science Foundation of China for Youths (no. 21601067), the Jiangsu Province Postdoctoral Science Foundation (no. 1601253C), and a Project Funded by the Priority Academic Program Development of Jiangsu Higher Education Institutions.

Conflict of interest

The authors declare no conflict of interest.

Keywords: electrochemistry · heterogeneous catalysis · nanostructures · transition metals · synthesis design

[1] M. H. Shao, Q. W. Chang, J. Dodelet, R. Chenitz, *Chem. Rev.* **2016**, *116*, 3594 – 3657.
[2] C. Z. Zhu, H. Li, S. F. Fu, D. Du, Y. H. Lin, *Chem. Soc. Rev.* **2016**, *45*, 517 – 531.
[3] M. Zhou, H. Wang, S. J. Guo, *Chem. Soc. Rev.* **2016**, *45*, 1273 – 1307.
[4] E. M. Miner, T. Fukushima, D. Sheberla, L. Sun, Y. Surendranath, M. Dincă, *Nat. Commun.* **2016**, *7*, 10942.
[5] D. Guo, R. Shibuya, C. Akiba, S. Saji, T. Kondo, J. Nakamura, *Science* **2016**, *351*, 361.
[6] C. Tang, Q. Zhang, *Adv. Mater.* **2017**, *29*, 1604103.
[7] Y. G. Li, H. L. Wang, L. M. Xie, Y. Y. Liang, G. S. Hong, H. J. Dai, *J. Am. Chem. Soc.* **2011**, *133*, 7296 – 7299.
[8] T. Palaniselvam, V. Kashyap, S. N. Bhange, J. Baek, S. Kurungot, *Adv. Funct. Mater.* **2016**, *26*, 2150 – 2162.
[9] L. Shang, H. J. Yu, X. Huang, T. Bian, R. Shi, Y. F. Zhao, G. I. N. Waterhouse, L. Wu, C. Tung, T. R. Zhang, *Adv. Mater.* **2016**, *28*, 1668 – 1674.
[10] H. Hu, L. Han, M. Z. Yu, Z. Y. Wang, X. W. Lou, *Energy Environ. Sci.* **2016**, *9*, 107 – 111.
[11] J. K. Li, S. Ghoshal, W. T. Liang, M. Sougrati, F. Jaouen, B. Halevi, S. McKinney, G. McCool, C. R. Ma, X. X. Yuan, Z. Ma, S. Mukerjee, Q. Y. Jia, *Energy Environ. Sci.* **2016**, *9*, 2418 – 2432.
[12] B. Cui, H. Lin, J. B. Li, X. Li, J. Yang, J. Tao, *Adv. Funct. Mater.* **2008**, *18*, 1440 – 1447.
[13] F. X. Ma, L. Yu, C. Y. Xu, X. W. D. Lou, *Energy Environ. Sci.* **2016**, *9*, 862 – 866.
[14] J. Wu, R. Mi, S. M. Li, P. Guo, J. Mei, H. Liu, W. Lau, L. Liu, *RSC Adv.* **2015**, *5*, 25304 – 25311.
[15] J. Pu, J. Wang, X. Q. Jin, F. L. Cui, E. H. Sheng, Z. H. Wang, *Electrochim. Acta* **2013**, *106*, 226 – 234.
[16] Z. Shi, L. Jiao, J. Sun, Z. Chen, Y. Chen, X. Zhu, J. Zhou, X. Zhou, X. Li, R. Li, *RSC Adv.* **2014**, *4*, 47 – 53.
[17] G. Q. Zhang, X. W. D. Lou, *Adv. Mater.* **2013**, *25*, 976 – 979.
[18] Y. Xiao, C. G. Hu, L. T. Qu, C. W. Hu, M. H. Cao, *Chem. Eur. J.* **2013**, *19*, 14271 – 14278.
[19] G. Q. Zhang, B. Y. Xia, X. Wang, X. W. Lou, *Adv. Mater.* **2014**, *26*, 2408 – 2412.
[20] X. L. Tong, S. Chen, C. X. Guo, X. H. Xia, X. Guo, *ACS Appl. Mater. Interfaces* **2016**, *8*, 28274 – 28282.
[21] G. D. Nie, X. F. Lu, M. Q. Chi, Y. Zhu, Z. Z. Yang, N. Song, C. Wang, *Electrochim. Acta* **2017**, *231*, 36 – 43.
[22] J. Yang, H. Y. Sun, H. Y. Liang, H. X. Ji, L. Song, C. Gao, H. X. Xu, *Adv. Mater.* **2016**, *28*, 4606 – 4613.
[23] C. L. Wang, X. Tan, J. T. Yan, B. Chai, J. F. Li, S. Z. Chen, *Appl. Surf. Sci.* **2017**, *396*, 780 – 790.
[24] K. R. Brown, A. P. Fox, M. J. Natan, *J. Am. Chem. Soc.* **1996**, *118*, 1154 – 1157.
[25] C. Comninellis, C. Pulgarin, *J. Appl. Electrochem.* **1993**, *23*, 108 – 112.
[26] Y. E. Miao, S. X. He, Y. L. Zhong, Z. Yang, W. W. Tjiu, T. X. Liu, *Electrochim. Acta* **2013**, *99*, 117 – 123.
[27] W. Tian, T. Y. Zhai, C. Zhang, S. L. Li, X. Wang, F. Liu, D. Q. Liu, X. K. Cai, K. Tsukagoshi, D. Golberg, Y. Bando, *Adv. Mater.* **2013**, *25*, 4625 – 4630.
[28] B. B. Wang, X. X. Fu, F. Liu, S. L. Shi, J. P. Cheng, X. B. Zhang, *J. Alloys Compd.* **2014**, *587*, 82 – 89.
[29] Y. D. Yin, R. M. Rioux, C. K. Erdonmez, S. Hughes, G. A. Somorjai, A. P. Alivisatos, *Science* **2004**, *304*, 711 – 714.
[30] X. F. Lu, D. J. Wu, R. Z. Li, Q. Li, S. H. Ye, Y. X. Tong, G. R. Li, *J. Mater. Chem. A* **2014**, *2*, 4706 – 4713.
[31] V. M. Jiménez, A. Fernández, J. P. Espinós, A. R. González-Elipe, *J. Electron Spectrosc. Relat. Phenom.* **1995**, *71*, 61 – 71.
[32] T. Choudhury, S. O. Saied, J. L. Sullivan, A. M. Abbot, *J. Phys. D* **1989**, *22*, 1185.
[33] R. L. Liu, C. von Malotki, L. Arnold, N. Koshino, H. Higashimura, M. Baumgarten, K. Müllen, *J. Am. Chem. Soc.* **2011**, *133*, 10372 – 10375.
[34] J. J. Yan, H. Y. Lu, Y. P. Huang, J. Fu, S. Y. Mo, C. Wei, Y. E. Miao, T. X. Liu, *J. Mater. Chem. A* **2015**, *3*, 23299 – 23306.
[35] C. Jin, F. L. Lu, X. C. Cao, Z. R. Yang, R. Z. Yang, *J. Mater. Chem. A* **2013**, *1*, 12170 – 12177.

Manuscript received: May 19, 2017
Revised manuscript received: July 10, 2017
Accepted manuscript online: July 12, 2017
Version of record online: August 15, 2017